Wideband Dual-Circularly-Polarized Reflect-Arrays Based on Dual-Functional-Layer Cells With Berry-Phase Compensation at X-Band

Yuan Li, Zhi Hao Jiang, Xuanfeng Tong, Fan Wu, Nan Shen, Ronan Sauleau, Wei Hong

▶ **To cite this version:**

Yuan Li, Zhi Hao Jiang, Xuanfeng Tong, Fan Wu, Nan Shen, et al.. Wideband Dual-Circularly-Polarized Reflect-Arrays Based on Dual-Functional-Layer Cells With Berry-Phase Compensation at X-Band. IEEE Transactions on Antennas and Propagation, 2022, 70 (10), pp.9924-9929. 10.1109/TAP.2022.3184536 . hal-03884485

HAL Id: hal-03884485
https://hal.science/hal-03884485

Submitted on 5 Jan 2023

HAL is a multi-disciplinary open access archive for the deposit and dissemination of scientific research documents, whether they are published or not. The documents may come from teaching and research institutions in France or abroad, or from public or private research centers.

L'archive ouverte pluridisciplinaire **HAL**, est destinée au dépôt et à la diffusion de documents scientifiques de niveau recherche, publiés ou non, émanant des établissements d'enseignement et de recherche français ou étrangers, des laboratoires publics ou privés.

Wideband Dual-Circularly-Polarized Reflect-Arrays Based on Dual-Functional-Layer Cells with Berry-Phase Compensation at *X*-band

Yuan Li, Zhi Hao Jiang, Xuanfeng Tong, Fan Wu, Nan Shen, Ronan Sauleau, and Wei Hong

***Abstract*—We present the design and experimental validation of wideband dual-circularly-polarized (dual-CP) reflect-arrays (RAs) based on dual-functional-layered unit cells with independent control of circular polarizations. The proposed dual-CP RA cells comprise a circular polarization selective surface (CPSS) on the top based on a bandwidth-enhanced dual-meandered Pierrot structure that implements polarization selection of CP waves and a reflective half-wave plate (HWP) on the bottom. The dual-CP phase delay of the RA cells relies on the Berry-phase dictated by the rotation of the CPSS and HWP elements for achieving reflective beamforming of CP waves of opposite handedness. The diffractive properties of an infinite periodic gradient array of the dual-CP RA cells in a triangular lattice are investigated, which numerically verifies the dual-CP anomalous reflection capability. Two proof-of-concepts operating at *X*-band are designed, fabricated, and characterized. By replacing only the bottom functional layer of the RA, symmetrical and asymmetrically-distributed dual-CP beams can be obtained. A measured peak gain of higher than 23.5 dBic is achieved, with a joint bandwidth of 11% for an axial ratio < 2 dB and a gain variation < 1 dB. The improved bandwidth performance, high-resolution BP compensation, and printed manufacturing process without using any metallic cavities make the demonstrated CPSS-based dual-CP RAs promising candidates for wireless observation and satellite communications.**

***Index Terms*—Dual-circularly-polarization, reflect-arrays (RAs), circular polarization selective surface (CPSS).**

I. INTRODUCTION

Circularly-polarized (CP) reflect-arrays (RAs) have attracted a lot of attention for their widespread usage in a variety of applications, such as earth observation, satellite communications, leveraged by their advantages of low misalignment-induced polarization mismatch and high transmission data rate [1]-[3]. Recent requirements in polarization multiplexing have led to the development of dual-circularly-polarized (dual-CP) RAs [4]. To date, three methods have been employed to realize RAs with dual-CP beamforming in the same frequency band.

The first approach makes use of a bottom dual-linear-polarized (dual-LP) reflector and a top circular polarizer that converts the dual-CP waves into two orthogonally polarized LP waves. In such a way, the dual-CP phase-compensation task is transformed into a dual-LP one [5], [6]. The phase shifting of the two orthogonal LP waves can be provided by a single-LP RA backed by a solid parabolic reflector [5] or a dual-LP RA with independent dynamic-phase (DP) compensation [6]. The dual-LP waves are then converted back into dual-CP beams by passing through the circular polarizer again. This interconversion makes the device subject to an intricate design procedure, certain efficiency reduction, and/or a larger RA panel thickness.

The second method utilizes the combination of Berry-phase (BP) and DP delays with a single functional layer. By rotating anisotropic elements, dual-CP RAs with independent dual-CP beam control can be achieved [7]-[11]. Such hybrid polarization-phase tuning methodology was presented for RA antenna designs in [8], which can generate adjacent pencil beams for two orthogonal CPs at 20 GHz with a 1.5 dB gain variation over a bandwidth of 7.6% and a peak antenna efficiency of 66%. However, the more precise the phase resolution is, the more types of cells with variable sizes [8], variable-length delay lines [9], and variable rotation angles are required, resulting in an increased complexity in the RA design process. Moreover, when it comes to circumstances that one of the dual-CP beams, with a certain handedness, needs to be altered, the entire RA must be re-designed and replaced since the structures for phase compensation of the two CP waves are physically linked to each other within each RA cell.

The third CP discrimination method uses two-functional-layer cells containing a circular polarization selective surface (CPSS) on the top and a CP reflective layer at the bottom. The CPSS performs the reflective beamforming of CP waves of one handedness and allows for the transmission of CP waves of the opposite handedness without any spatially varying phase delays, whereas the bottom layer is responsible for the control of the CP beam of the opposite handedness. The CPSS structure, as a critical component of this type of dual-CP RAs, was initially proposed and investigated by Pierrot in 1966 for CP wave reflection [12], but its resonant structure inevitably results in narrowband operation. Modifications of the Pierrot cells in terms of implementation strategies have been investigated, such as using a single-layer substrate [13], [14] and loaded vertical segments [15], for eliminating the metallic vias. However, the bandwidth of these modified CPSS is still too narrow for practical usage. In [16], a CPSS with an enhanced -1 dB bandwidth of 11% was demonstrated experimentally based on a low-permittivity and low-loss substrate. In addition to CP discrimination, the capability of CPSS for reflective wavefront shaping has also been exploited by introducing BP into the cells [17], [18]. Aside from the CPSS, half-wave plate (HWP) structures can also reflect CP waves with a maintained handedness due to the 180° phase difference between the reflected LP waves along the two optical axes of the cells. Therefore, the HWP cells with BP compensation have been widely employed in CP RAs for realizing single-CP beams with a high polarization purity [1], [3]. By combining CPSS and HWP structures in a cascaded fashion, dual-CP RA cells have been proposed and verified [19], [20]. Moreover, CPSS-based 2 × 2 bit dual-CP RAs with a 9.4% bandwidth of AR < 3.5 dB and gain variation < 1.5 dB were reported in [21]. Similarly, these dual-CP cells/RAs still suffer from their intrinsic narrow bandwidth and large panel thickness. Besides, metallic cavities are utilized to isolate elements for mutual coupling reduction [19]-[21], which results in a heavier weight and more complicated assembly process. Also, the unstable angular response and low phase resolution due to element miniaturization leads to a high AR of the generated beams.

In this communication, we report the design of CPSS-based dual-CP RAs based on dual-functional-layer cells with only BP compensation with an improved bandwidth and higher polarization purity. By

Manuscript received May 31th, 2022. This work was supported in part by National Natural Science Foundation of China (NSFC) under Grant 62122019 and 61901106, in part by the High Level Innovation and Entrepreneurial Research Team Program in Jiangsu, and in part by the ZTE Corporation and State Key Laboratory of Mobile Network and Mobile Multimedia Technology. (*Corresponding author: Zhi Hao Jiang.*)

Y. Li, X. F. Tong, and F. Wu are with the State Key Laboratory of Millimeter Waves, School of Information Science and Engineering, Southeast University, Nanjing 210096, China.

Z. H. Jiang and W. Hong are with the State Key Laboratory of Millimeter Waves, School of Information Science and Engineering, Southeast University, Nanjing 210096, China, and also with Purple Mountain Laboratories, Nanjing 211111, China (e-mail: zhihao.jiang@seu.edu.cn).

N. Shen is with the State Key Laboratory of Mobile Network and Mobile Multimedia Technology, ZTE Corporation, Shanghai, China.

R. Sauleau is with Univ Rennes, CNRS, IETR (Institut d'Electronique et des Technologies du numéRique) - UMR 6164, F-35000 Rennes, France.

Accepted manuscript

proposing miniaturized and bandwidth-broadening RA cells and employing a triangular array lattice, wideband dual-CP beamforming relying on continuous BP compensation can be achieved. Comparing to those reported in [19]−[21], this work exhibits significant improvements in bandwidth performance and unit-cell angular response, which has additional advantages of reduced weight and thickness of the RA panel due to the elimination of metallic cavity walls. Two illustrative RAs with different beam distributions are demonstrated by simply replacing the second functional layer, verifying its layer-substitutable capability.

This communication is organized as follows. In Section II, the configuration of the RA, the design and scattering properties of the RA cells are presented. Section III reports the diffraction characteristics and reflective wave deflection behavior of a linear phase gradient array composed of the proposed RA cells. In Section IV, the simulated and experimental results of two proof-of-concept RAs with symmetrical and asymmetrical dual-CP beams are shown. Finally, the conclusions are drawn in Section V.

II. RA Configuration and Element Designs

A. Dual-CP RA Configuration

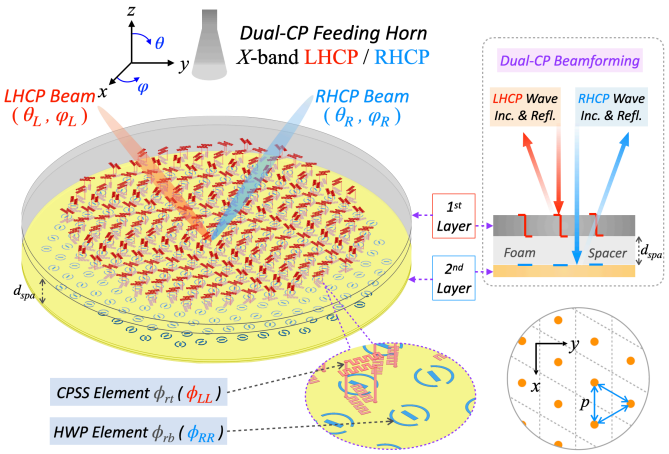

Fig. 1. Configuration of the dual-CP RA composed of two functional layers reflecting LHCP and RHCP waves, respectively. The inset shows the detail view of the RA panel. The schematic reveals elements are arranged in an equilateral triangular lattice with a periodicity p = 13.86 mm.

The proposed dual-CP RA operates at *X*-band (around 11.0 GHz). It is composed of a first functional layer on the top and a second functional layer placed on the bottom (Fig. 1). These layers contain CPSS and HWP cells with spatially-dependent in-plane rotation angle distributions of $\phi_{rt}(x,y)$ and $\phi_{rb}(x,y)$, respectively. They are separated by a polymethacrylimide (PMI) foam spacer with a thickness of d_{spa} = 20 mm, as introduced in [21]. An *X*-band dual-CP feeding horn is used to illuminate the RA, generating a left-hand circularly polarized (LHCP) beam reflected by the first functional layer pointing at (θ_L, φ_L) and a right-hand circularly polarized (RHCP) beam formed by the second functional layer directing at (θ_R, φ_R), respectively. The directions of the dual-CP beams can be independently selected; they are determined by the rotation angle distribution of the cells in the two functional layers, respectively. An equilateral triangular lattice is chosen in both functional layers for a more compact elements arrangement, a wider beam scanning coverage, and a broader bandwidth as compared to a RA with conventional square lattice. The maximum scanning angles of a triangular grid array and a square grid array satisfy the following relationship [22]

$$\theta_{tr}/\theta_{sq} = \sin^{-1}\left(\frac{1.155\lambda}{p} - 1\right)/\sin^{-1}\left(\frac{\lambda}{p} - 1\right) \quad (1)$$

Eq. (1) shows that the triangular grid array exhibits a larger scanning angle with the same period p. In other words, such an array architecture is more amenable for wide-angle applications.

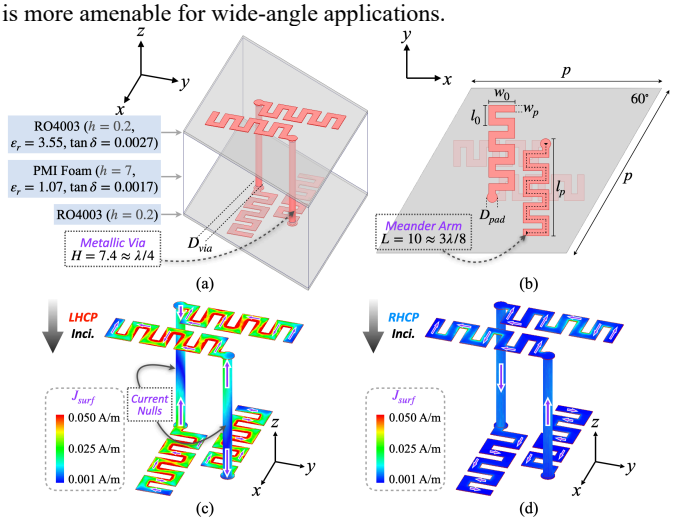

Fig. 2. (a) 3-D view and (b) top view of the CPSS unit-cell. The geometrical dimensions (in millimeters) are the following: D_{via} = 0.5, D_{pad} = 0.75, w_p = 0.5, l_p = 7.13, w_0 = 1.9, l_0 = 1.45, and p = 13.86. Simulated surface current distributions of the dual-meandered Pierrot structure under the illumination of (c) LHCP and (d) RHCP waves.

B. CPSS Cell Design

Evolved from the conventional Pierrot structure [13], a dual-meandered Pierrot structure is proposed and employed for the first functional layer [see Fig. 2(a) and (b)]. This CPSS cell consists of two Rogers 4003 substrates patterned with two sets of orthogonally oriented meandered metallic arms and a quarter-wavelength thick PMI foam layer sandwiched in between them for providing mechanical support [21]. The two sets of metallic arms, with a length of $L \approx 3\lambda_0/8$, are interconnected by a metallic via, resulting in a total length of the crank-like shaped metallic structure of about $1\lambda_0$. The dual-meandered Pierrot structure with a two-fold rotational symmetry is placed in a

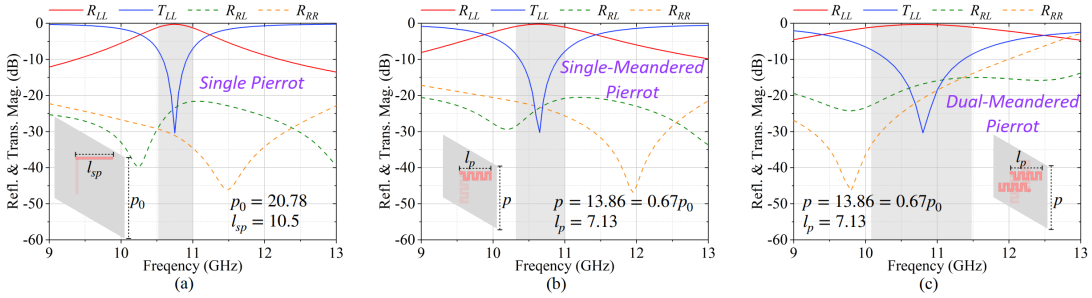

Fig. 3. Simulated *S*-parameters of (a) conventional CPSS cell based on single Pierrot structure, (b) miniaturized CPSS cell based on single-meandered Pierrot structure, and (c) modified CPSS cell based on dual-meandered Pierrot structure. The inset shows the planar views of the CPSS cells. The geometrical dimensions are all in millimeters. The shaded region indicates the 1-dB band of R_{LL}.

Accepted manuscript

rhombic-shaped cell with a side length of p = 13.86 mm, i.e., about $\lambda_0/2$, and a 60° included angle. The simulated reflection and transmission magnitudes of the proposed CPSS cells are represented in Fig. 4(a) and (b) as a function of frequency. Numerical simulations have been carried out using a high-frequency structure simulator (HFSS). The magnitudes of the co-polarized LHCP reflection (R_{LL}) and RHCP transmission (T_{RR}) are above -1 dB in the frequency range of 10.1 – 11.5 GHz and 9.0 – 12.1 GHz with a peak of -0.32 and -0.08 dB, respectively.

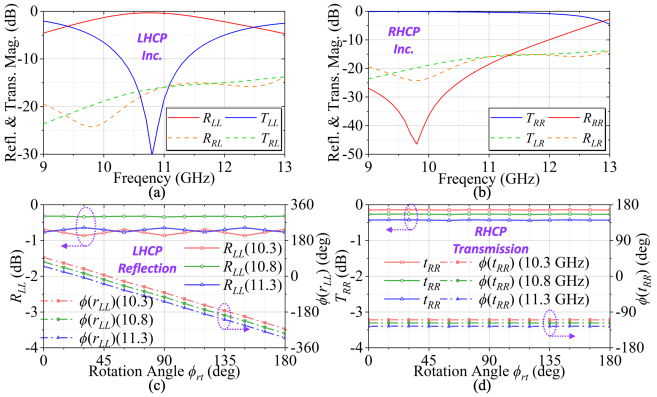

Fig. 4. Simulated CP reflection and transmission magnitudes of the CPSS cells under the excitation of (a) LHCP and (b) RHCP waves. (c) Simulated R_{LL} and $\phi(r_{LL})$ of the CPSS cell as a function of rotation angle ϕ_{rt}. (d) Simulated T_{RR} and $\phi(t_{RR})$ of the CPSS cell as a function of rotation angle ϕ_{rt}.

In contrast to the conventional Pierrot structure, whose operational principle has been explained in [19] and [20], the dual-meandered Pierrot structure with a two-folded rotational symmetry can make a better use of the space within a unit cell. Since the two single configurations are 180°-symmetric with each other, an out-of-phase current distribution can be observed on the two configurations. When it is illuminated by the LHCP/RHCP wave, in-phase/out-of-phase currents are stimulated on the horizontal metallic arms of the same single-meandered configuration, causing the resonance/non-resonance of the entire configuration, exhibiting reflective/transparent to the corresponding incident wave [see Fig. 2(c) and (d)]. This modification provides an enhanced CP discrimination performance with negligible mutual-interaction, manifested by an extended bandwidth due to the increased spatial density of cells in comparison with the single-meandered configuration [15].

A comparison between these CPSS configurations is illustrated in Fig. 3. The configuration and scattering parameters of the conventional Pierrot structure with strip arms and single-meandered Pierrot structure are shown in Fig. 3(a) and (b), where a 30% cell size reduction and an extended 1-dB R_{LL} bandwidth (6.6% compared to 4.2%) can be observed due to the utilization of meandered arms. In comparison, the unit cell performance of the proposed dual-meandered Pierrot structure is displayed in Fig. 3(c). Without additional size enlargement, this arrangement keeps a proper distance between intra-cell and inter-cell vertical conductors, which avoids the undesired mutual-coupling, thereby resulting in a significantly enhanced 1-dB bandwidth of R_{LL} (about 13%) and a more robust angular response.

Apart from the performance in CP discrimination, BP delay can be introduced to obtain reflective phase shifting for LHCPs, simply by rotating the CPSS element. The simulated R_{LL} and T_{RR}, along with the co-polarized CP phases, i.e., $\phi(r_{LL})$ and $\phi(t_{RR})$, are provided in Fig. 4(c) and (d) as a function of cell rotation angle ϕ_{rt} at several frequencies. It can be seen that a linear phase progression can be observed in $\phi(r_{LL})$, while R_{LL} is kept at a high level larger than -1 dB. In contrast, the T_{RR} and $\phi(t_{RR})$ remain almost unchanged as the CPSS cell rotates.

To conclude, the CPSS cells on the first functional layer allow manipulating the reflection phase of the incident LHCP wave with pre-defined BP delays, while they transmit the RHCP wave with a negligible impact.

C. HWP Cell Design

To provide beamforming for RHCP waves, the elements on the bottom functional layer should have anisotropic scattering properties exhibiting a 180° phase difference between the LP reflected waves polarized along the two optical axes of the elements. The configuration of the HWP cell is shown in Fig. 5. It contains two Rogers 4003 substrates sandwiching a Rogers 4450F bonding film. Metallic patterns are etched on the topmost of substrate, while the ground plane is placed on the lowermost of the substrate. A unit-cell containing two split arcs with a short dipole located at the center is adopted, which offers a better performance in terms of size-reduction, polarization purity, and wide bandwidth than cells with a single arc or dipole [2].

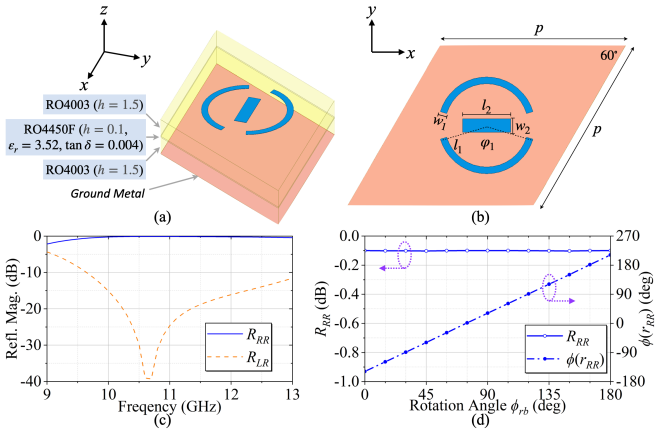

Fig. 5. (a) 3-D view and (b) top views of the HWP cell. The geometrical dimensions (in millimeters) are the following: l_1 = 7.2, w_1 = 0.5, l_2 = 3.6, and w_2 = 1, the angle φ_1 = 147°. (c) Simulated R_{RR} and R_{LR} of the HWP cell. (d) Simulated R_{RR} and $\phi(r_{RR})$ of the HWP cell as a function of rotation angle ϕ_{rb}.

The simulated co-polarized RHCP reflection is plotted in magnitude in Fig. 5(c). It can be seen that in the band from 10.0 to 12.2 GHz, the co-polarized reflection magnitude (R_{RR}) is higher than -0.3 dB, while the cross-polarized reflection (R_{LR}) is below -15 dB, indicating a high polarization discrimination. Similarly, by rotating the HWP element, a linear phase change can be achieved for the RHCP reflection waves as the cell rotates around its center while maintaining the reflection magnitude better than -0.1 dB [see Fig. 5(d)]. As a summary, the HWP cells on the second functional layer allows tuning the reflection phase of the incident RHCP wave with BP compensation.

D. Cascaded Dual-Functional-Layer RA Cell

For dual-CP RAs with more than one functional layer, it is essential to ensure that the response of each layer is well-maintained when all the functional layers are cascaded. Hence, the mutual effect of the two functional layers on the dual-CP reflective properties of the cascaded cells are evaluated by utilizing a multi-layer transmission line model, where the 20-mm-thick PMI foam spacer is included [see Fig. 6(a)].

Firstly, the generalized scattering matrices (GSMs) in LP basis of the cells are obtained for each functional layer. The transfer matrix of the PMI foam spacer sandwiched between the two layers can be readily acquired once its permittivity and thickness are known. By using the transformation between S-parameters and $ABCD$ matrix, the S-parameters of the entire cascaded RA cell can be calculated by cascading the transmissive structure A (a combination of the CPSS cell and foam spacer) and the reflective structure B (the HWP cell)

$$[\boldsymbol{S}]_{11}^{tot} = [S]_{11}^{A} + [S]_{12}^{A} \cdot [S]_{11}^{B} \cdot [S]_{21}^{A} \cdot (\boldsymbol{I} - [S]_{22}^{A} \cdot [S]_{11}^{B})^{-1} \quad (2)$$

Accepted manuscript

where [***S***] is the 2 × 2 *S*-parameters tensor in the LP basis and ***I*** is the identity matrix.

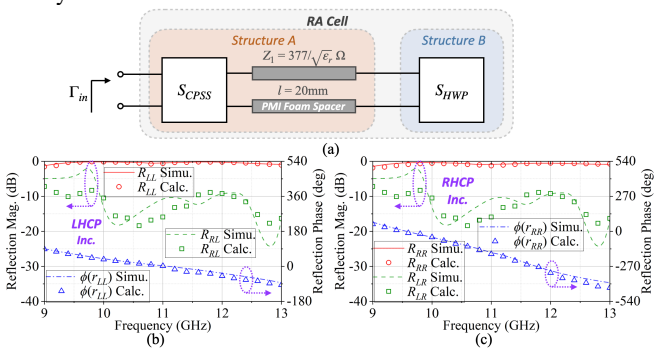

Fig. 6. (a) Transmission line model of the cascaded dual-functional-layer RA cell. Simulated and calculated CP reflection magnitudes and phases with (b) LHCP and (c) RHCP illumination.

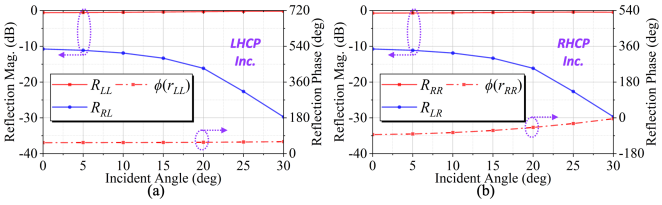

Fig. 7. Simulated CP reflection magnitudes and phases for RA cell as a function of incident angles with (b) LHCP and (c) RHCP illumination.

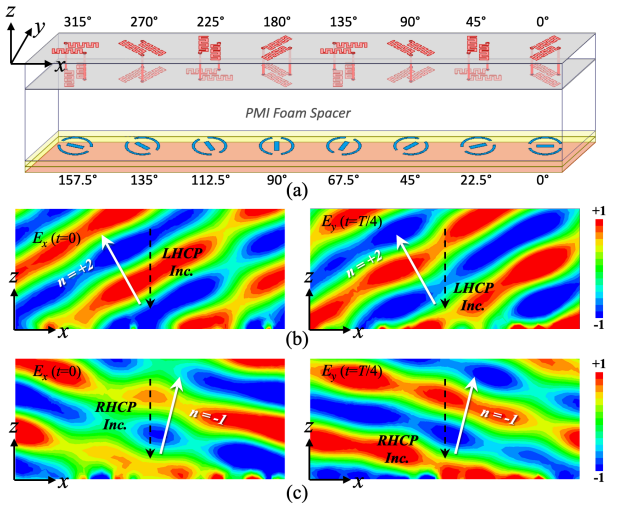

Fig. 8. (a) Configuration of the supercell. Snapshots of the simulated scattered electric fields (E_x at $t = 0$ and E_y at $t = T/4$) when the supercell is illuminated by a normally incident (b) LHCP and (c) RHCP wave at 11 GHz.

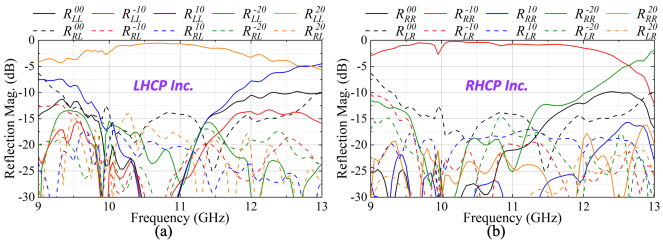

Fig. 9. Simulated CP reflection magnitudes of the supercell as a function of frequency for different diffraction modes with (a) LHCP and (b) RHCP illumination.

The GSM of the cascaded structure is converted into CP basis and compared to that obtained from the full-wave simulation that takes into account the near-field inter-layer coupling. The CP reflection magnitudes and phases are displayed in Fig. 6(b) and (c). As it can be seen, the calculated reflection responses are in good agreement with the simulated result in the targeted band, revealing that the inter-layer coupling is very weak. This implies that the beamforming for LHCP and RHCP waves can be decomposed into two independent tasks fulfilled by the two functional layers, respectively, which greatly simplifies the design of the integrated RAs.

E. Oblique Incidence Performance of the Dual-CP RA Cell

Since the cells on the outmost of the proposed RA are illuminated by oblique-incident waves with a maximum incident angle of 29°, the angular response of the RA cells is investigated. For the LHCP case, when the incident angle varies from 0° to 30°, the variation of R_{LL} remains lower 0.4 dB while R_{RL} declines gradually and $\phi(r_{LL})$ remains almost unchanged [see Fig. 7(a)]. Similar effects can be observed in the RHCP [see Fig. 7(b)], except for $\phi(r_{RR})$ that varies by about 90° when the incident angle increases. These phase responses can be readily taken into consideration during the RA design process.

III. Diffraction Analysis of a Supercell With Gradient Phase

Before designing the final RAs, the diffraction properties of an infinite periodic supercell composed of several CP reflective cells with a gradient phase are investigated. As shown in Fig. 8(a), the supercell consists of eight CPSS and HWP cells aligned along the *x*-direction with a rotation angle gradient of 45° and 22.5°, respectively. Master/slave periodic boundaries and Floquet ports are used to simulate an infinite array environment with a triangular lattice.

The snapshots of the simulated distributions of the scattered electric field components at different instantaneous times, i.e., E_x at $t = 0$ and E_y at $t = T/4$, are shown Fig. 8(b) and (c). As it can be seen, when a normally incident LHCP plane wave illuminates the supercell, a reflected LHCP wave is diffracted into the +2nd-order mode with a deflection angle of $\theta_{rLL} = 29°$. In contrast, with a RHCP incident plane wave, the reflected RHCP wave couples into the -1st-order diffraction mode with the beam tilting at $\theta_{rRR} = -14°$. The simulated LHCP/RHCP reflection magnitudes into different polarizations and diffraction modes as a function of frequency are present in Fig. 9. In the band from 10.1 to 11.7 GHz, the co-polarized LHCP and RHCP reflection magnitudes are higher than −1 dB for the desirable diffraction modes, i.e., R_{LL}^{20} and R_{RR}^{-10}, while the reflection magnitudes of the unwanted other modes are all below -12 dB. The numerical results of supercell corroborate well with those obtained from the generalized law of reflection, revealing that the cells on the two functional layers enables efficient dual-CP wave deflection in an inhomogeneous array environment.

IV. Dual-CP RA Designs and Experiments

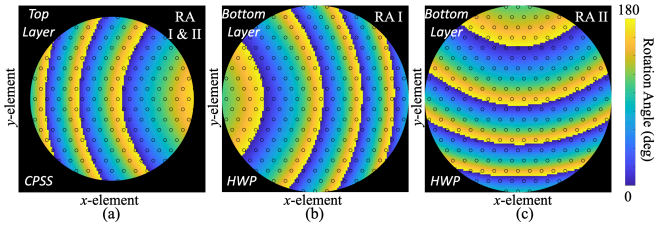

Fig. 10. Element rotation angle distribution on the two functional layers of the RA I and II. The black circles denote the center of the CPSS and HWP element's location.

Based on the proposed RA cells, two proof-of-concept *X*-band dual-CP RAs with different beam directions are designed and demonstrated. Both RAs are composed by 186 CPSS cells and 238 HWP cells. The number of HWP cells has been increased to account for the additional loss caused when the RHCP wave propagates through the first

Accepted manuscript

functional layer. An *X*-band conical dual-CP horn with a gain of 18 dBic and a -10 dB beamwidth of 38° is used to illuminate the RA. The *F*/*D* ratio is set to be 0.95 such that the incident angle for the outermost cell is about 29°, resulting in a focal distance of 200 mm. During the design, the simulated field distributions of the waves emitted from the horn at both functional layers are utilized to determine the required LHCP and RHCP phase compensation.

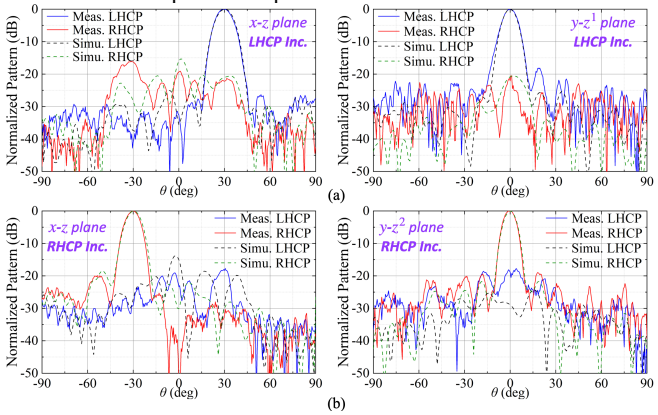

Fig. 11. Simulated and measured normalized CP radiation patterns of RA I in the two orthogonal planes passing through the main beam: (a) LHCP and (b) RHCP feed, where $\hat{z}^1 = \hat{z}cos30^o + \hat{y}sin30^o$ and $\hat{z}^2 = \hat{z}cos30^o - \hat{y}sin30^o$.

A. Dual-CP RA Designs

As shown in Fig. 1, the panel of RA I is composed of the top CPSS layer and bottom HWP layer, which are separated by a PMI foam spacer. By adjusting the in-plane rotation angle of the elements on two functional layers, RA I can generate LHCP and RHCP beams symmetrically distributed in the x-z plane pointing at (30°, 0°) and (30°, 180°), respectively. The cell rotation angle distribution on the two functional layers of the RA I are presented in Fig. 10 (a) and (b). The simulated normalized CP patterns at 11 GHz in the two orthogonal main-beam planes, i.e., *x*-*z* / *y*-*z*^{1} planes and *x*-*z* / *y*-*z*^{2} planes, are shown in Fig. 11. When the RA is excited by the LHCP waves, a directive LHCP beam is generated pointing at 30° in the *x*-*z* plane. Likewise, when the feeding horn operates in RHCP mode, a RHCP beam pointing at -30° in the *x*-*z* plane is obtained. The simulated cross-polarization levels at the beam center are below -20 dB for both CP beams. The simulated gain and AR for the dual-CP beams are represented as a function of frequency in Fig. 12(a) and (b); they exhibit a joint 1-dB gain and AR < 2 dB bandwidth of 19.6% and 15.7%, respectively. The simulated peak gain values of the LHCP and RHCP beams reach 23.6 and 23.2 dBic, corresponding to aperture efficiencies of about 38.5% and 29%, respectively.

RA II shares almost the same configuration with that of RA I. The only change is that the bottom functional layer, i.e., the HWP layer, is replaced by a new one with the HWP elements rotation rearranged [see Fig. 10(c)]. Since negligible coupling can be observed between these two functional layers, the substitution of the bottom HWP layer would hardly affect the performance of the top CPSS layer. As a result, the direction of the RHCP beam is changed to (30°, 90°), while the direction of the LHCP beam remains unchanged. The simulated normalized CP patterns at 11 GHz in the *x*-*z* / *x*-*z*^{1} plane and *y*-*z* / *x*-*z*^{3} plane are represented in Fig. 13. An LHCP and RHCP beam pointing at 30° in the *x*-*z* and *y*-*z* planes are obtained, respectively. The simulated cross-polarization levels at the beam center are also well below -20 dB. The simulated gain and AR of the LHCP and RHCP beams are displayed in Fig. 12(c) and (d), showing a joint 1-dB gain and AR < 2 dB bandwidths of 14.7% and 16.1%, respectively. The simulated peak LHCP and RHCP gain values are 23.38 and 23.27 dBic, indicating aperture efficiencies of about 36.5% and 29.6%, respectively.

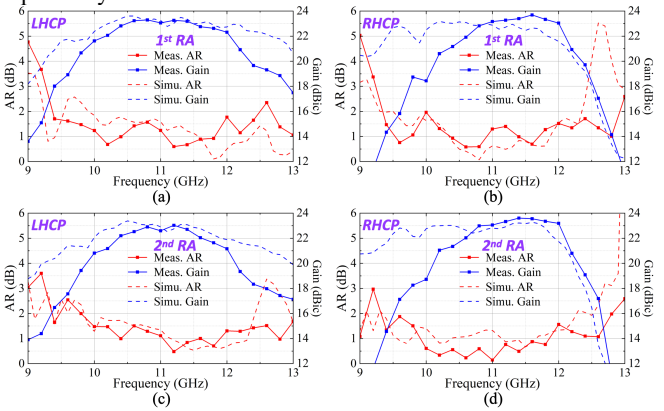

Fig. 12. Simulated and measured peak gain and AR as a function of frequency for the (a) LHCP and (b) RHCP beams of RA I, and LHCP and (d) RHCP beams of RA II.

B. Experimental Results

Both dual-CP RA have been fabricated and assembled. First, the two thin substrates of the first functional later are fixed on the top and bottom surfaces of a 7mm-thick PMI foam layer using Teflon screws. Through holes are drilled in both the substrates and foam at positions where the vertical metallic vias need to be placed connecting the horizontal arms of the dual-meandered Pierrot structures. Then the first and second functional layer as well as a PMI foam spacer are combined using Teflon screws. Fig. 14(a) displays the RA prototype installed on a glass frame, with the insets showing the enlarged views of the portion of the two functional layers. The two dual-CP RAs are measured in a far-field anechoic chamber [see Fig. 14(b)].

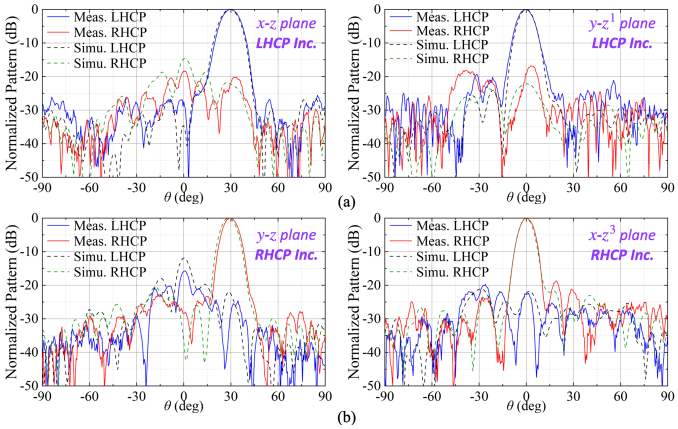

Fig. 13. Simulated and measured normalized radiation patterns of RA II in the two orthogonal planes passing through the main beam: (a) LHCP and (b) RHCP feed, where $\hat{z}^1 = \hat{z}cos30^o + \hat{y}sin30^o$ and $\hat{z}^3 = \hat{z}cos30^o + \hat{x}sin30^o$.

The measured normalized CP radiation patterns in the *x*-*z* / *y*-*z*^{1} plane and *x*-*z* / *y*-*z*^{2} plane of RA I are represented in Fig. 11. The measured data are in good agreement with the simulated results. The measured sidelobe levels (SLLs) and cross-polarization levels of the LHCP/RHCP beam equal -18/-19 dB and -20/-18 dB, respectively. The measured joint 1-dB gain and AR < 2 dB bandwidths for the two beams are 15.2% and 11.3% [see Figs. 11(a) and (b)]. The measured peak gain values reach 23.3 and 23.7 dBic for LHCP and RHCP beams, corresponding to aperture efficiencies of 31.6% and 30.0%.

For RA II, the measured normalized CP radiation patterns in the *x*-*z* / *x*-*z*^{1} plane and *y*-*z* / *x*-*z*^{3} plane are plotted in Fig. 13, exhibiting SLLs and cross-polarization levels of -20/-19 dB and -18/-22 dB for the LHCP/RHCP beam. The measured joint 1-dB gain and AR < 2 dB

Accepted manuscript

TABLE I. A COMPARISON AMONG DIFFERENT CP RAS BASED ON CPSS

	Return loss of CPSS cells (1-dB Bandwidth)	AR of CPSS Reflection	Thickness of CPSS	Dual-CP Beamforming	Total thickness of panel	*F/D*	Phase Resolution	Gain & AR Bandwidth of Dual-CP Beams	Aperture Efficiency
[21]	< 1 dB (4.3%)	2.2 dB	8.49 mm ($0.24\lambda_0$)	Yes	66.9 mm ($1.9\lambda_0$)	0.8	1.92 bit	9% / 9%* (Gain var. < 1.5 dB, AR < 3.5dB)	25%
[17]	0.4 dB (\)	3 dB	4 mm ($0.15\lambda_0$)	No	N.A.	N.A.	>2 bit	N.A.	N.A.
[18]	0.69 dB (< 8.3%)	1.2 dB	9.55 mm ($0.38\lambda_0$)	No	N.A.	N.A.	Continuous	N.A.	N.A.
RA I	0.32 dB (14.8%)	2.1 dB	7.4 mm ($0.25\lambda_0$)	Yes	30.7 mm ($1\lambda_0$)	0.95	Continuous	15% / 11% (Gain var. < 1 dB, AR < 2dB)	29%~ 38.5%
RA II	0.32 dB (14.8%)	2.1 dB	7.4 mm ($0.25\lambda_0$)	Yes	30.7 mm ($1\lambda_0$)	0.95	Continuous	12% / 11% (Gain var. < 1 dB, AR < 2dB)	29.6%~ 36.5%

* The data before "/" is for LHCP beam and after "/" is for RHCP beam.

bandwidths are 11.9% and 11.4% for the LHCP and RHCP beams [see Fig. 12(c) and (d)]. Measured peak gains of 23.0 and 23.6 dBic for LHCP and RHCP beams are achieved, indicating measured aperture efficiencies of 27.4% and 30.4%.

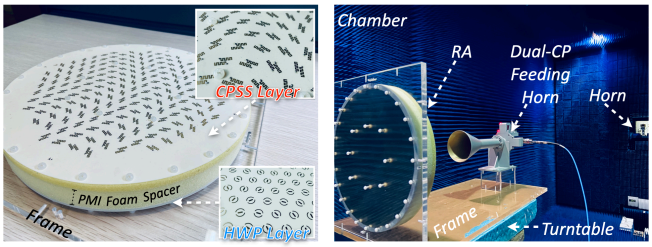

(a) (b)

Fig. 14. (a) Photographs of the fabricated dual-CP RA prototype fixed on a glass frame. (b) Measuring environment of the RA in a far-field chamber.

A comparison between the proposed dual-CP RAs and other previously reported CP elements/RAs based on CPSS structures and BP compensation is shown in Table I. It can be seen that this work has superiority in bandwidth, performance, and structural complexity.

V. CONCLUSION

In summary, the design and experiments of dual-CP RAs based on dual-functional-layer cells and entirely relying on BP compensation are presented. The proposed RAs contain two substitutable functional layers that reflect and modulate LHCP and RHCP incident waves, respectively. Two exemplary dual-CP RAs are synthesized and fabricated for demonstration, showing measured results in a good agreement with the simulated ones. By employing the dual-meandered Pierrot CPSS cells and triangular array lattice, an enhanced operational bandwidth and more robust angular response can be achieved. Both RAs possess a joint 1-dB gain and AR < 2 dB bandwidth of wider than 11%. Such simplification in structure and improvements in both the bandwidth and polarization purity make this dual-CP RAs amenable for wireless and space applications.

REFERENCE

[1] C. Han *et al.*, "A C/Ka dual frequency dual layer circularly polarized reflectarray antenna with microstrip ring elements," *IEEE Trans. Antennas Propag.*, vol. 52, no. 11, pp. 2871-2876, Nov. 2004.

[2] A. Yu, F. Yang, A. Z. Elsherbeni, J. Huang, and Y. Kim, "An offset-fed X-Band reflectarray antenna using a modified element rotation technique," *IEEE Trans. Antennas Propag.*, vol. 60, no. 3, pp. 1619-1624, Mar. 2012.

[3] M.-Y. Zhao *et al.*, "Design of new single-layer multiple-resonance broadband circularly polarized reflectarrays," *IEEE Antennas Wireless Propag. Lett.*, vol. 12, pp. 356–359, 2013.

[4] G.-B. Wu, S.-W. Qu, S. Yang, and C. H. Chan, "Broadband, single layer dual circularly polarized reflectarrays with linearly polarized feed," *IEEE Trans. Antennas Propag.*, vol. 64, no. 10, pp. 4235–4241, Oct. 2016.

[5] M. Joyal, R. El Hani, M. Riel, Y. Demers, and J. Laurin, "A reflectarray-based dual-surface reflector working in circular polarization," *IEEE Trans. Antennas Propag.*, vol. 63, no. 4, pp. 1306-1313, Apr. 2015.

[6] C. S. Geaney, M. Hosseini, and S. V. Hum, "Reflectarray antennas for independent dual linear and circular polarization control," *IEEE Trans. Antennas Propag.*, vol. 67, no. 9, pp. 5908-5918, Sep. 2019.

[7] X. Zhang *et al.*, "Hybrid polarization-phase tuning methodology for reflectarray antennas," *IEEE Trans. Antennas Propag.*, early access.

[8] R. Florencio *et al.*, "Flat reflectarray that generates adjacent beams by discriminating in dual circular polarization," *IEEE Trans. Antennas Propag.*, vol. 67, no. 6, pp. 3733–3742, Jun. 2019.

[9] Z. H. Jiang, Y. Zhang, and W. Hong, "Anisotropic impedance surface-enabled low-profile broadband dual-circularly polarized multibeam reflectarrays for Ka-band applications," *IEEE Trans. Antennas Propag.*, vol. 68, no. 8, pp. 6441-6446, Aug. 2020.

[10] Z. H. Jiang, T. Yue, and W. Hong, "Low-profile and wideband dual-circularly-polarized reflect-arrays based on rotated metal-backed dual-polarized aperture-coupled patch elements," *IEEE Trans. Antennas Propag.*, vol. 68, no 3, pp. 2108-2117, Mar. 2020.

[11] W. Guo *et al.*, "Dual-phase hybrid metasurface for independent amplitude and phase control of circularly polarized wave," *IEEE Trans. Antennas Propag.*, vol. 68, no. 11, pp. 7705–7710, May. 2020.

[12] R. Pierrot, "Eléments résonants en polarisation circulaire et réflecteur semi-transparent composé de ces éléments," *French Patent* No. 89.609, 1.512.598, Dec. 30, 1966.

[13] I-Y. Tarn *et al.*, "A new advance in circular polarization selective surface–A three layered CPSS without vertical conductive segments," *IEEE Trans. Antennas Propag.*, vol. 55, no. 2, pp. 460–467, Feb. 2007.

[14] I. Lopez and J.-J. Laurin, "A circular polarization selective surface implemented on a flexible substrate," *IEEE Trans. Antennas Propag.*, vol. 62, no. 7, pp. 3887–3852, Jul. 2014.

[15] I. Lopez and J. J. Laurin, "Alternative topologies of circular polarization selective surfaces based on modifications of the Pierrot cell," *IEEE Trans. Antennas Propag.*, vol. 63, no. 4, pp. 1465–1472, Apr. 2015.

[16] J. Sanz-Fernández, E. Saenz, and P. de Maagt, "A circular polarization selective surface for space applications," *IEEE Trans. Antennas Propag.*, vol. 63, no. 6, pp. 2460–2470, Jun. 2015.

[17] T. Cai *et al.*, "Bifunctional Pancharatnam-Berry metasurface with high-efficiency helicity-dependent transmissions and reflections," *Annalen Der Phys.*, vol. 530, 2017, Art. no. 1700321.

[18] M. Kim *et al.*, "Design and experimental demonstration of impedance-matched circular-polarization-selective surfaces with spin-selective phase modulations," *Phys. Rev. Appl.*, vol. 13, pp. 014009, Jan. 2020.

[19] S. Mener *et al.*, "Design and characterization of a CPSS-based unit-cell for circularly polarized reflectarray applications," *IEEE Trans. Antennas Propag.*, vol. 61, no. 4, pp. 2313–2318, Apr. 2013.

[20] S. Mener, R. Gillard, R. Sauleau, C. Cheymol, and P. Potier, "Unit cell for reflectarrays operating with independent dual circular polarizations," *IEEE Antennas Wireless Propag. Lett.*, vol. 13, pp. 1176–1179, 2014.

[21] S. Mener *et al.*, "Dual circularly polarized reflectarray with independent control of polarizations," *IEEE Trans. Antennas Propag.*, vol. 63, no. 4, pp. 1877–1881, Apr. 2015.

[22] A. K. Bhattacharyya, *Phased Array Antennas: Floquet Analysis, Synthesis, BFNs and Active Array Systems*, vol. 179. Hoboken, NJ, USA: Wiley, 2006.

Accepted manuscript